

## Orbital imaging and spectroscopy using $s$ -NIXS

Liu Hao Tjeng<sup>#</sup>, Andrea Amorese, Brett Leedahl, Andrea Severing, Martin Sundermann

The search for new strongly correlated quantum materials is often focused on materials containing transition-metal, rare-earth and/or actinide elements. Understanding the behavior of the  $d$  and  $f$  electrons involved is hereby essential. The identification of the active  $d$  or  $f$  orbitals has so far been mostly deduced from optical, x-ray and neutron spectroscopies in which spectra must be analyzed using theory or modelling. This, however, is also a challenge in itself, since *ab-initio* calculations hit their limits due to the many-body nature of the problem. Here we developed a new experimental method that circumvents the need for complex analysis and instead provides the information as measured. With this technique, we can make a direct image of the active orbital and determine what the atomic-like object looks like in a real solid [1, 2]. The method,  $s$ -core-level non-resonant inelastic X-ray scattering ( $s$ -NIXS), relies on high momentum transfer in the inelastic scattering process, which is necessary for dipole-forbidden terms ( $s \rightarrow d$ ,  $s \rightarrow f$ ) to gain spectral weight. Moreover, we are able to utilize  $s$ -NIXS for the study of the excited states [3]: by obtaining images we can identify the orbital character of those excited states, which in turn facilitates the extraction of important energy parameters in the strongly correlated materials.

### Motivation to develop charge-neutral spectroscopies involving $s$ core levels.

The spectral intensity of the dipole-allowed  $s \rightarrow p$  transition depends on the orientation of the electric field polarization vector of the photon relative to the orientation of the  $p$  orbital. Because the  $s$  orbital is spherically symmetric, sweeping the polarization vector over all angles yields an angular intensity distribution that directly maps the shape and orientation of the  $p$ -orbital hole. Our objective is to apply this procedure also to  $d$  and  $f$  orbitals. However,  $s \rightarrow d$  or  $s \rightarrow f$  transitions are dipole-forbidden and therefore cannot be accessed using established photo-absorption spectroscopies. We have to resort to experimental methods that have non-vanishing matrix elements beyond the dipole limit. This is our motivation to explore the possibilities of x-ray Raman or non-resonant inelastic X-ray scattering (NIXS) spectroscopy, which became available with modern high-brilliance synchrotron facilities.

### Direct imaging of orbitals in quantum materials.

(H. Yavaş, M. Sundermann, K. Chen, A. Amorese, A. Severing, H. Gretarsson, M. W. Haverkort, and L. H. Tjeng [1]).

The interaction of light with matter is given by two terms: a term proportional to the scalar product of the electron momentum operator  $\mathbf{p}$  and the photon vector potential  $\mathbf{A}$ , and a term proportional to the vector potential  $\mathbf{A}$  squared. When the photon energy matches an atomic resonance, the  $\mathbf{p} \cdot \mathbf{A}$  term dominates; off-resonance, the interaction is governed by the  $\mathbf{A}^2$  term. NIXS is non-resonant so that the last term matters and the double differential cross-section  $d^2\sigma/d\Omega d\omega$  becomes proportional to the dynamical structure factor

$S(\mathbf{q}, \omega)$ , which contains the material-specific information we are seeking.

Here  $|i\rangle$  and  $|f\rangle$  denote the (many-body) initial and final

$$S(\mathbf{q}, \omega) = \sum_f |\langle f | e^{i\mathbf{q} \cdot \mathbf{r}} | i \rangle|^2 \delta(\hbar\omega_i - \hbar\omega_f - \hbar\omega)$$

states,  $\mathbf{q} = \mathbf{k}_i - \mathbf{k}_f$  the transferred momentum,  $\hbar\omega = \hbar\omega_i - \hbar\omega_f$  the transferred energy, and  $\mathbf{k}_{i,f}$  and  $\hbar\omega_{i,f}$  the momentum and energy of the incoming and scattered photons, respectively.

Beyond-dipole matrix elements appear in the scattering cross-section when expanding the transition operator  $e^{i\mathbf{q} \cdot \mathbf{r}}$  to the  $k^{\text{th}}$  order, where  $k$  denotes the multipole order of the scattering cross-section. The so-called triangular condition and parity rule restrict the number of multipoles to  $|l_f - l_i| \leq k \leq l_f + l_i$  and  $|l_i + l_f + k| = \text{even}$  for the  $l_i \rightarrow l_f$  transition (respective orbital momenta of the initial and final states). This implies that for a  $d \rightarrow f$  transition, only dipole ( $k=1$ ), octupole ( $k=3$ ) and triakontadipole ( $k=5$ ) scattering orders occur, and that for  $s \rightarrow d$  transitions (dipole-forbidden) only the quadrupole term with  $k=2$  contributes to  $S(\mathbf{q}, \omega)$ .

For small momentum transfers  $|\mathbf{q}|$ , NIXS and dipole-allowed x-ray absorption spectroscopy (XAS) spectra very much look alike. In other words, the NIXS  $2p/3p \rightarrow 3d$  excitations in transition-metal compounds or the  $3d/4d \rightarrow 4f/5f$  and  $5d \rightarrow 5f$  excitations in rare-earth and actinide materials exhibit line shapes that are very similar to the ones obtained from x-ray absorption spectroscopy (XAS). The only difference is that in NIXS, the direction of the momentum transfers  $\hat{\mathbf{q}} = \mathbf{q}/|\mathbf{q}|$  provides the information that is obtained from the electrical vector polarization in XAS. However, for large  $|\mathbf{q}|$ , for the same metal ion, the  $p \rightarrow d$  or  $d \rightarrow f$

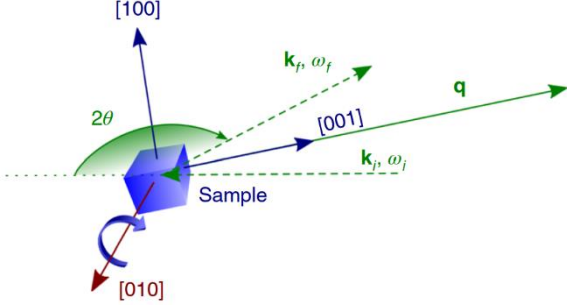


Fig. 1: Scattering geometry of the experiment. This geometry, which outlines the scattering triangle, remains fixed throughout the measurements. The single crystal sample (blue) is rotated around an axis perpendicular to the scattering plane (maroon) by an angle  $\varphi$ , and for each  $\varphi$  an inelastic spectrum is collected. Here,  $\varphi = 0$  refers to  $\mathbf{q} \parallel [001]$  (specular geometry).

transitions yield a different spectral distribution with additional features that cannot be seen in a dipole-based XAS experiment. Moreover, the dipole-forbidden  $s \rightarrow d$  or  $s \rightarrow f$  transitions (quadrupolar or octopolar, respectively) now have non-vanishing matrix elements, and consequently are allowed and become visible.

We investigated the  $s \rightarrow d$  transition of a single crystal of NiO, an antiferromagnetic insulator, with the Ni  $d^8$  configuration. In our experimental set-up, as illustrated in Fig. 1,  $S(\mathbf{q}, \omega)$  of the NiO sample was recorded as a function of the sample angle  $\varphi$ , here defined as the angle between the fixed momentum transfer vector  $\mathbf{q}$  and the NiO surface normal.

Fig. 2 shows a compilation of NIXS spectra measured for many different sample angles. The spectra show the  $M_{2,3}$  edge ( $3p \rightarrow 3d$ ) of nickel at around 70 eV energy transfer and, most importantly, the dipole-forbidden  $M_1$  ( $3s \rightarrow 3d$ ) excitations at around 110 eV, overlaid on

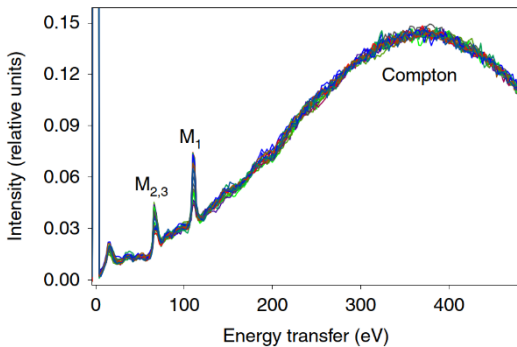


Fig. 2: Experimental non-resonant inelastic X-ray scattering spectra of NiO containing the core level excitations on top of the Compton profile.

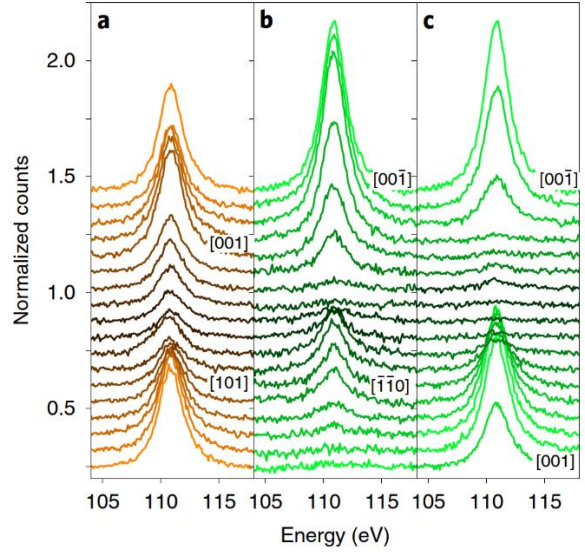


Fig. 3: Close-up view of the experimental Ni  $M_1$  ( $3s \rightarrow 3d$ ) edge spectra for different sample rotations and orientations.

the broad Compton profile. The signal-to-background ratio is excellent in the energy range of the  $M_1$  edge. A close-up of this edge and its directional dependence of vector  $\mathbf{q}$  from  $\mathbf{q} \parallel [001]$  to  $\mathbf{q} \parallel [100]$  are displayed in Fig. 3a, and for  $\mathbf{q}$  from  $\mathbf{q} \parallel [001]$  to  $\mathbf{q} \parallel [110]$  in Fig. 3b,c. In the close-up plots, the Compton profile has been subtracted using a simple linear background.

We then determined the integrated intensity of each spectrum in Fig. 3 and placed it on a polar plot as displayed in Fig. 4. Figure 4a shows the data points for  $\mathbf{q}$  sweeping in the  $[001]$ – $[100]$  plane (orange) and Fig. 4b for  $\mathbf{q}$  in the  $[001]$ – $[110]$  plane (green). They fall accurately on top of the orbital shapes, which denote ‘cuts’ through the  $[001]$ – $[100]$  (orange) and  $[001]$ – $[110]$  (green) planes of the calculated three-dimensional (3D) orbital hole density (square of the wavefunction) of the Ni high-spin  $3d^8$  configuration in octahedral coordination, namely the  ${}^3A_2$   $3d_{(x^2 - y^2)}3d_{(3z^2 - r^2)}$  as shown in Fig. 4c. The fundamental information that we have obtained is extremely detailed; for example, we can clearly see the small lobes of the  $3d_{(3z^2 - r^2)}$  contribution in Fig. 4b. We note that the  $3d_{(x^2 - y^2)}$  contribution vanishes in the  $[001]$ – $[110]$  plane (Fig. 4b), while both  $3d_{(x^2 - y^2)}$  and  $3d_{(3z^2 - r^2)}$  contribute in the  $[001]$ – $[100]$  plane (Fig. 4a).

This means that we have developed a purely experimental method that can directly visualize atomic-like quantum mechanical objects in solids. The directional dependence of the integrated  $s$ -NIXS intensity at the Ni  $M_1$  edge ( $3s \rightarrow 3d$ ) directly maps the local orbital hole density of the ion in the ground state.

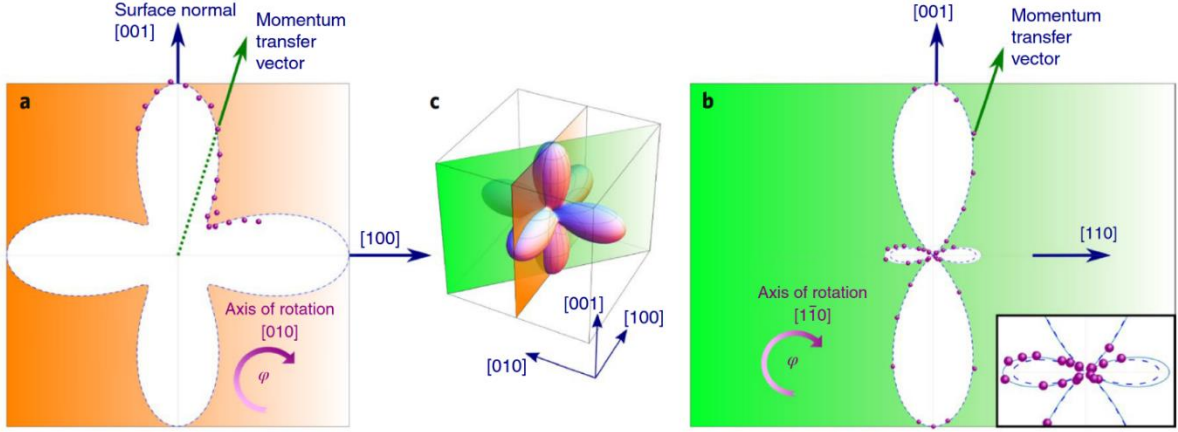


Fig. 4: Integrated intensities of  $M_1$  ( $3s \rightarrow 3d$ ) edge spectra plotted on the projections of the orbital shape of the  ${}^3A_2 3d_{(x^2-y^2)}3d_{(3z^2-r^2)}$  hole density.

There is no need to carry out analysis of the spectral line shape to extract this information, in contrast to, for example, the non- $s$  edges  $L_{2,3}$  [4],  $M_{4,5}$  [5],  $N_{4,5}$  [6], and  $O_{4,5}$  [7]. The reason is fundamental: the  $M_1$  ( $3s \rightarrow 3d$ ) quadrupolar excitation involves a spherically symmetric  $s$  orbital, so that the angular distribution of the intensity is solely determined by the hole charge distribution in the initial state with respect to  $\mathbf{q}$ . We emphasize that details of the  $s$ -NIXS final states do not matter since the information is extracted from the integrated intensity of the spectra i.e. from all final states. As a result, only the properties of the initial state are probed. The latter is true for both localized and itinerant systems.

**Origin of Ising magnetism in  $\text{Ca}_3\text{Co}_2\text{O}_6$  unveiled by orbital imaging.** (B. Leedahl, M. Sundermann, A. Amorese, A. Severing, H. Gretarsson, L. Zhang, A. C. Komarek, A. Maignan, M. W. Haverkort, and L. H. Tjeng [2]).

The cobaltate  $\text{Ca}_3\text{Co}_2\text{O}_6$  is an intriguing material having an unconventional magnetic structure, displaying quantum tunneling phenomena in its magnetization. One-dimensional chains are formed in the crystal along the  $c$ -axis with alternating  $\text{CoO}_6$  octahedra and trigonal prisms (see Fig. 5). In the  $ab$ -plane, the chains form a triangular-type lattice, and the intra-chain Co–Co coupling is ferromagnetic, while the inter-chain coupling is antiferromagnetic. The unusual magnetic properties, along with its highly Ising-like character are linked to the geometrically frustrated crystal lattice.

The origin of the Ising magnetism as well as the charge and spin states of the two Co sites are subject of an ongoing discussion. All of the previous studies relied on calculations of one type or another, with varying

and conflicting outcomes, depending on what theoretical approach was used. To resolve these issues, we have applied  $s$ -NIXS, relying on its ability to make a direct image of the active  $3d$  orbitals in real space.

We can identify two sets of spectra in our  $s$ -NIXS data: a higher energy set and a lower energy set (not shown). The third panel of Fig. 6 shows the polar plot of the higher energy spectra (green dots). We take the *Ansatz* that this four-lobe entity originates from the octahedral Co ions and that these are in the  $3+$  charge and low-spin (LS) state, i.e.  $3d^6$  with a  $t_{2g}^6$  configuration as depicted in the first panel of Fig. 6. This implies that the four holes of the octahedral Co ion will be in the  $e_g$  shell, as displayed in the second panel of Fig. 6. It is necessary to consider the crystal structure in more detail in order to explain the asymmetries in the four-lobe shape: (1) along the Co–Co chains there are alternating octahedral Co sites that are rotated  $45^\circ$  about the  $c$ -axis from one another; (2) the axes along which the lobes lay for the two sites are oriented  $13.5^\circ$  off right angles from one another. Both of these are apparent in Fig. 5.

Following these considerations, we sum up  $e_g^4$  holes of the two sites and plot the respective cut on top of the experimental data (see solids line in Fig. 6 middle).

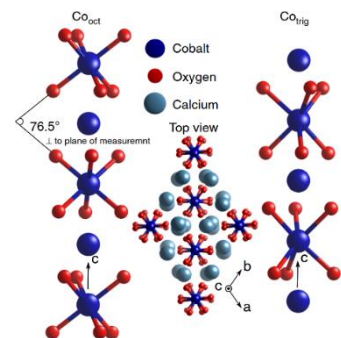


Fig. 5: Crystal structure of  $\text{Ca}_3\text{Co}_2\text{O}_6$ .

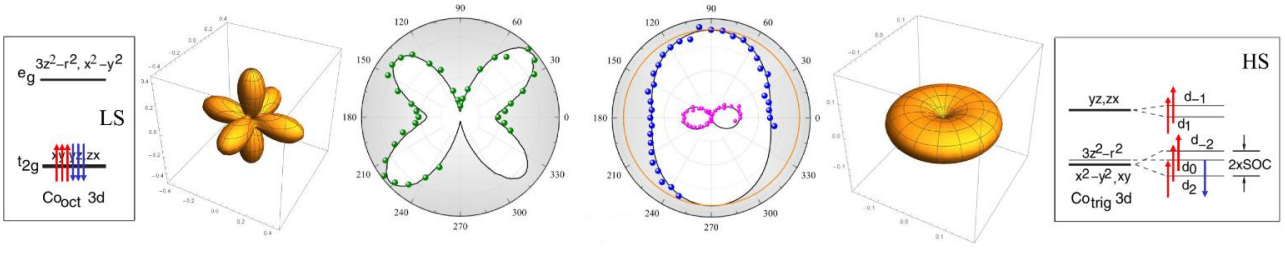


Fig. 6: (left panels) octahedral Co: one-electron energy diagram,  $e_g^4$  hole density,  $s$ -NIXS polar plot; (right panels) trigonal prismatic Co:  $s$ -NIXS polar plot, sixth electron density, one-electron energy diagram.

The near-perfect agreement establishes that this *Ansatz* is correct, i.e. that the octahedral Co ions are 3+ and nonmagnetic. Any different *Ansatz* (for example 3+ high-spin, or 2+ high-spin) results in a clear mismatch with the experiment.

The finding of the 3+ charge state for the octahedral Co implies that the trigonal prismatic Co is also 3+ to fulfil the charge balance of the  $\text{Ca}_3\text{Co}_2\text{O}_6$  chemical formula. Since the octahedral Co is LS nonmagnetic, the trigonal prismatic Co must carry the entire magnetic moment of the compound. The  $s$ -NIXS polar plot as displayed in the fourth panel of Fig. 6 (blue dots) must therefore reflect the hole density of a high-spin (HS)  $3d^6$  ion. Realizing that the hole density of a HS  $3d^5$  ion is spherical (see red circle in the same panel), we can determine the orbital of the sixth (minority-spin) electron of the trigonal prismatic Co ion by subtracting the measured  $s$ -NIXS hole density from the HS  $3d^5$  hole density. The result is depicted by the magenta dots. We now can directly "see" that it is a slice through a donut-shaped orbital as shown in the fifth panel of Fig. 6 (the  $s$ -NIXS data in a slice perpendicular to the  $c$ -axis reveal circularly shaped polar plots). This donut is the well-known complex  $d_2$  orbital that carries  $2\mu_B$  orbital momentum making the system highly Ising like. It is quite rare that the complex  $d_2$  orbital can be stabilized in an oxide, making the prismatic trigonal coordination rather unique.

In summary, the direct orbital imaging capability of  $s$ -NIXS allows us to unambiguously solve the complex charge, spin, and Ising problem of  $\text{Ca}_3\text{Co}_2\text{O}_6$ .

**Selective orbital imaging of excited states with x-ray spectroscopy: the example of  $\alpha$ -MnS.** (A. Amorese, B. Leedahl, M. Sundermann, H. Gretarsson, Z. Hu, H.-J. Lin, C. T. Chen, M. Schmidt, H. Borrmann, Yu. Grin, A. Severing, M. W. Haverkort, and L. H. Tjeng [3]).

In the previous  $s$ -NIXS studies we have made use of the integrated intensity of the spectra to extract information about the orbital occupation in the ground

state. We have not made use of the spectral line shape. In this study, we will look at what information can be extracted from the analysis of the *excited states* and how the orbital imaging capability of  $s$ -NIXS can be of value. To this end we investigated the local electronic structure of MnS, a Mn  $3d^5$  high-spin system with orbital degrees of freedom in the excited states.

The left panel of Fig. 7 shows a compilation of the Mn  $M_1$  ( $3s \rightarrow 3d$ ) NIXS spectra measured for a range of sample orientations. The integrated intensity does not vary with the orientation angle. The hole density of the Mn ion is thus isotropic, fully consistent with the spherical charge shape of the half-filled  $3d$  shell of the high-spin  $\text{Mn}^{2+}$  material. The peak position of the spectra, however, varies considerably with orientation.

We take this as an indication for the presence of  $3s^1 3d^6$  excited states having different energies. The right panel of Fig. 7 displays how we decompose a spectrum at a given orientation in terms of a  $\mathbf{q} \parallel [111]$  (blue dots) and  $\mathbf{q} \parallel [001]$  (orange dots) spectra, thereby making use of the observation that these two spectra have the lowest and highest peak energies, respectively.

We now make polar plots of the  $\mathbf{q} \parallel [111]$  and  $\mathbf{q} \parallel [001]$  components as function of the MnS crystal orientation,

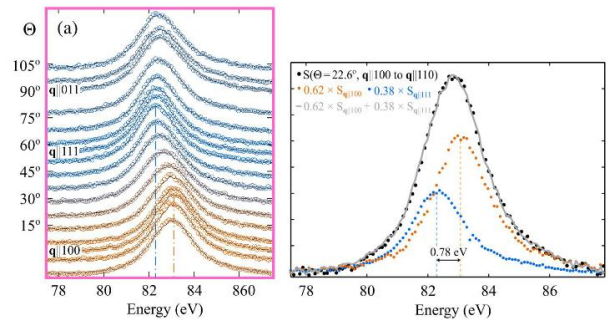


Fig. 7: (left panel) experimental Mn  $M_1$  ( $3s \rightarrow 3d$ ) edge spectra of MnS for different sample orientations; (right panel) decomposition in terms of weighted sums of  $\mathbf{q} \parallel [111]$  (blue) and  $\mathbf{q} \parallel [001]$  (orange dots) spectra.

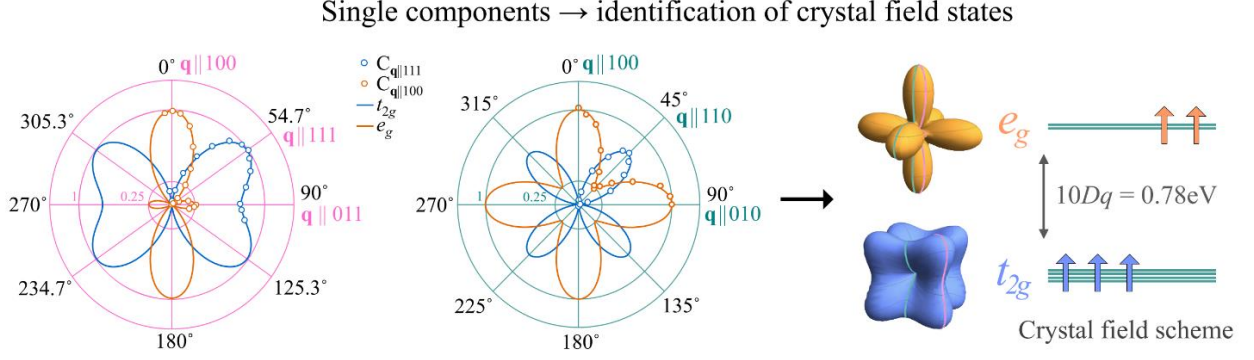


Fig. 8: The intensity of the  $\mathbf{q}||[111]$  (blue dots) and  $\mathbf{q}||[001]$  (orange dots) components follow the angular dependence of the  $t_{2g}$  (blue) and  $e_g$  (orange) orbitals, respectively. The  $t_{2g}$ - $e_g$  energy splitting is  $10Dq=0.78$  eV.

see Fig. 8. It turns out that the angular dependence follows the shape of the  $t_{2g}$  and  $e_g$  orbitals with great accuracy, allowing us to directly identify the orbital character of the excited states. The energy difference between these two states is due to the  $t_{2g}$ - $e_g$  splitting, and it is therefore a direct measurement of the crystal-field parameter  $10Dq = 83.15$  eV –  $82.37$  eV =  $0.78$  eV.

A proper interpretation of the spectra must include the effect of Coulomb and exchange interactions between the electrons within the  $d$  shell, meaning that we need to put our results in a many-body framework which considers both the full atomic multiplet theory and the local effect of the lattice. In particular, starting from the high-spin  $3s^23d^5$  configuration for the ground state of the Mn ion in  $\alpha$ -MnS, the  $s$ -NIXS process leads to a  $3s^13d^6$  final state. Since the  $s$  core hole does not add an extra orbital angular momentum component, the multiplet structure of the final state will be closely related to the one of the  $3d^6$  configuration. Therefore, we can make use of the well-established Sugano-Tanabe-Kamimura diagrams for a quantitative analysis of the spectra, after including modifications due to the exchange interaction with the extra  $3s$  spin:

$$H_{3s-3d}^{\text{Coulomb}} = -\frac{2}{5}\hat{\mathbf{S}}_d \cdot \hat{\mathbf{S}}_s G_{3s-3d}^2 + n_d \left( F_{3s-3d}^0 - \frac{1}{10} G_{3s-3d}^2 \right).$$

The resulting energy diagram is shown in Fig. 9. It is important to realize that selection rules dictate that only two states can be reached from the high-spin  $3d^5$  ground state, and these two are the  ${}^5T_{2g}$  and  ${}^5E_g$  as marked by the yellow stars in Fig. 9. The  $10Dq$  value can be determined from their energy separation.

A dramatically different spectrum would be observed if the system were low spin  $3d^5$ : five states were spread over a very large energy range of about 6 eV. Our experimental data that show two closely lying peaks thus reconfirm that the Mn in MnS is high spin  $3d^5$ .

We have also investigated the influence of covalency on the  $s$ -NIXS image of the local  $d$  hole density. To this end, we have carried out configuration interaction calculations using an octahedral  $\text{MnS}_6$  cluster which includes explicitly the hybridization between the Mn  $3d$  and the S  $3p$  orbitals. We have set the hopping integrals for the  $e_g$  orbital at 1.92 eV and for the  $t_{2g}$  at 1.15 eV, and varied the energy difference between the  $3d^5$  and  $3d^6\bar{L}$  configurations, i.e. the charge transfer energy  $\Delta$ . Here  $\bar{L}$  denotes the S  $3p$  ligand hole states. The results are shown in Fig. 10.

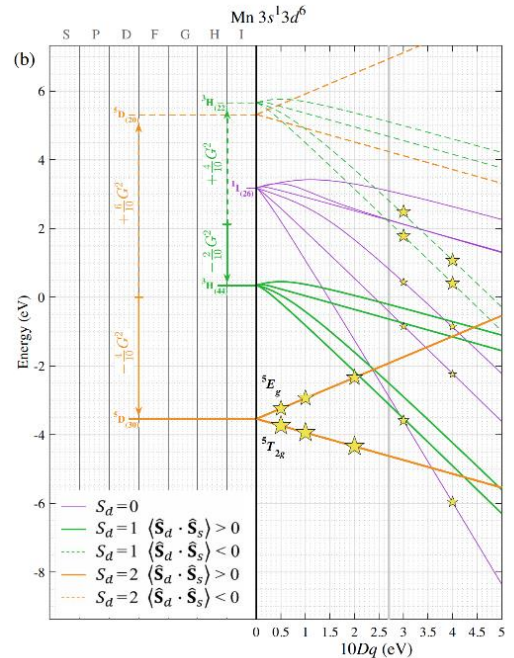


Fig. 9: Subsection of the modified Sugano-Tanabe-Kamimura diagram for a  $3s^13d^6$  ion. Stars indicate the possible final states of the  $s$ -NIXS process. The vertical line at  $10Dq \approx 2.7$  eV is the border between the high- and low-spin configurations of the  $3d^5$  ground state.

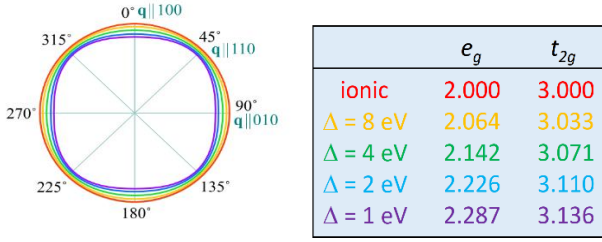


Fig. 10: *s*-NIXS hole density and occupation numbers for the  $e_g$  and  $t_{2g}$  subshells as function of covalency.

Starting with the ionic calculation, we have for the ground state an electron occupation of 3.000 for the  $t_{2g}$  orbital and 2.000 for the  $e_g$ . The corresponding ground state hole density is spherical. Switching on the hybridization, the electron occupation in the ground state increases when lowering the  $\Delta$  values. The occupation increases faster for the  $e_g$  than for the  $t_{2g}$ , consistent with the fact that the hopping integral with the ligand is larger for the  $e_g$  than for the  $t_{2g}$ . Accordingly, the ground state hole density, proportional to the NIXS signal, decreases for lower  $\Delta$  values and becomes strongly non-spherical (left-hand panel). This also means that the amount of hybridization can be extracted from the precise shape of the hole density as measured by *s*-NIXS.

In conclusion, we have shown that *s*-NIXS has also the unique ability to directly provide a spatial image of the local excited states of transition metal ions, thereby simplifying the identification of the multiplet character of those states. We have further shown that the well-established Sugano-Tanabe-Kamimura diagrams can be used for the analysis of the spectra since the *s* core hole does not add an extra orbital angular momentum. The present studies demonstrate that the analysis of *s*-NIXS spectra provides (1) the character of the excited states, (2) the relevant energy parameters, and (3) the character of the ground state. In addition, the integrated *s*-NIXS spectra also give (4) direct information about the character of the ground state. Information (4) can then be used to check the information obtained from (3). Alternatively, in case the spectra are extremely complex, information (4) can be used as a constraint for the analysis of the spectra so that (1) and (2) can be

extracted more reliably. Therefore *s*-NIXS opens up new opportunities to determine the local electronic structure in a wide range of transition metal compounds.

### External Cooperation Partners

M.W. Haverkort, Heidelberg University. MPI agreement with DESY-PETRA-III for beamline P01.

### References

- [1]\* *Direct imaging of orbitals in quantum materials*, H. Yavaş, M. Sundermann, K. Chen, A. Amorese, A. Severing, H. Gretarsson, M. W. Haverkort, and L. H. Tjeng, *Nature Physics* **15** (2019) 559.
- [2]\* *Origin of Ising magnetism in  $\text{Ca}_3\text{Co}_2\text{O}_6$  unveiled by orbital imaging*, B. Leedahl, M. Sundermann, A. Amorese, A. Severing, H. Gretarsson, L. Zhang, A. C. Komarek, A. Maignan, M. W. Haverkort, and L. H. Tjeng, *Nature Communications* **10** (2019) 5447.
- [3]\* *Selective orbital imaging of excited states with x-ray spectroscopy: the example of  $\alpha\text{-MnS}$* , A. Amorese, B. Leedahl, M. Sundermann, H. Gretarsson, Z. Hu, H.-J. Lin, C. T. Chen, M. Schmidt, H. Borrmann, Yu. Grin, et al., *Physical Review X* **11** (2021) 011002.
- [4] *c-axis dimer and its electronic breakup: the insulator-to-metal transition in  $\text{Ti}_2\text{O}_3$* , C. F. Chang, T. C. Koethe, Z. Hu, J. Weinen, S. Agrestini, L. Zhao, J. Gegner, H. Ott, G. Panaccione, H. Wu, et al., *Phys. Rev. X* **8** (2018) 021004.
- [5] *Correlation between ground state and orbital anisotropy in heavy fermion materials*, T. Willers, F. Strigari, Z. Hu, V. Sessi, N. B. Brookes, E. D. Bauer, J. L. Sarrao, J. D. Thompson, A. Tanaka, S. Wirth, et al., *PNAS* **112** (2015) 2384.
- [6] *4f crystal field ground state of the strongly correlated topological insulator  $\text{SmB}_6$* , M. Sundermann, H. Yavas, K. Chen, D. J. Kim, Z. Fisk, D. Kasinathan, M. W. Haverkort, P. Thalmeier, A. Severing, and L. H. Tjeng, *Phys. Rev. Lett.* **102** (2018) 016402.
- [7]\* *From antiferromagnetic and hidden order to Pauli paramagnetism in  $\text{UM}_2\text{Si}_2$  compounds with 5f electron duality*, A. Amorese, M. Sundermann, B. Leedahl, A. Marino, D. Takegami, H. Gretarsson, A. Gloskovskii, C. Schlueter, M. W. Haverkort, Y. Huang, et al., *PNAS* **117** (2020) 30220.

#hao.tjeng@cpfs.mpg.de